POLITECNICO
MILANO 1863

MSc in Aeronautical Engineering
Course of **Spacecraft Propulsion**

Liquid Rocket Engine design, analysis and simulation

Alessandro Del Bono 993719
Paolo Bux 968118
Serkan Gemalmaz 961927
Sooraj Gunasekar 969784
Máté-Erik Moni 968436
Giulio Morandi 101009
Chiara Pasquariello 989942
Antonio Pucciarelli 974675
M Jihad Ummul Quro 974843

Academic year **2021/2022**

Abstract

This report aims at presenting an early study of a new propulsion system, initially sized to provide a nominal thrust of $100N$. The system consists of a bi-propellant liquid rocket engine with a blow-down architecture. The combustion chamber of the engine is made of Inconel 718 with additive layer manufacturing. First of all, a short overview of liquid rocket engines and additive manufacturing technology is given. Then, given the constraints, the nominal thermodynamic parameters are computed, from which it is possible to complete the design of the engine. A simulation of the combustion is then performed, in order to evaluate the evolution of the performances during the burning time, and to understand if the chosen design is able to fulfill the requirements. Lastly, the uncertainties on the design are discussed, focusing in particular on the management of additive manufacturing layers and on how their properties affect the production. A Monte Carlo analysis is performed in order to define the uncertainty boundaries due to the production and to understand their impact on the thrust. Critical observations are also made regarding the scaling up (1000N thrust engine) and down (10N thrust engine) of the system and how the manufacturing uncertainties affect them.

Nomenclature

α	conical nozzle what type of angle
$\bar{T}$	Monte Carlo simulation mean thrust value
β	convergent nozzle angle
Δp_p	pressure drop across the feeding pipe
Δp_v	pressure drop across the valve
ΔP_{cool}	pressure drop across the cooling system
ΔP_{inj}	pressure drop across the injector
$\dot{m}$	mass flow rate
$\dot{m}_{OX}$	$H_2O_2 + H_2O$ mass flow rate
$\dot{m}_{RP-1}$	RP-1 mass flow rate
$\frac{O}{F}$	oxidizer to fuel ratio
λ	nozzle 3D loss coefficient
ϕ_{OX}	$H_2O_2 + H_2O$ injection plate holes diameter
ϕ_{RP-1}	$RP-1$ injection plate holes diameter
ρ	density
σ_T	Monte Carlo simulation standard deviation value
θ_e	Rao nozzle exit angle
θ_i	Rao nozzle initial angle
ε	expansion ratio
A	reference area
A_c	combustion chamber cross sectional area
A_t	throat area
A_{inj}	injector area
AM	additive manufacturing
c^*	characteristic velocity
C_D	discharge coefficient
c_T	thrust coefficient
D_p	feeding pipe diameter
f_p	feeding pipe friction coefficient

I_{sp}	specific impulse
k	specific heat ratio
k_v	valve pressure drop coefficient
L^*	characteristic length
L_p	feeding pipe length
L_{conv}	nozzle convergent part length
L_{div}	nozzle divergent part length
m	mass
M_c	combustion chamber Mach number
M_{mol}	propellant molar mass
N_{inj}	number of injectors
P_e	nozzle exit pressure
P_{CC}	combustion chamber pressure
Q	volumetric flow rate
r_c	combustion chamber radius
r_e	nozzle exit radius
r_t	throat radius
T	instantaneous thrust
t_b	burn time
T_{CC}	combustion chamber temperature
U_f	velocity in the feed line
V_c	combustion chamber volume

Contents

List of Figures

List of Tables

Chapter 1

Introduction

1.1 Review of LRE, propellant injection and combustion

A liquid rocket engine consists of a combustion chamber, a feed mechanism for supplying the propellants from their tanks to the combustion chamber, a power source to maintain the energy for the feed mechanism, suitable piping to transfer the liquid propellants under pressure, a structure to transmit the thrust force, and control devices (including valves). Liquid propellants are either expelled from their tanks by a high-pressure gas or they are delivered by pumps to the thrust chambers.

The combustion chamber is the place where the liquid propellants are injected, atomized, mixed, and then burned. After this process, hot gaseous reaction products are formed. The gaseous products are accelerated and ejected at high velocities to obtain thrust. In regenerative cooling combustion chambers, one of the propellants (usually the fuel) is circulated through cooling jackets to diminish the heat transfer from the hot reaction gases to the combustion chamber walls.

Small Liquid Rocket Engines (SLRE) are commonly used for auxiliary propulsion that is used in trajectory adjustments and attitude control. Some of the characteristics of SLRE can be summarized as the following. Generally, they have a low total impulse. The thrust level is small, and it can be between $0.001N$ and $4500N$. The pressurization system is a pressurized feed system with high pressure gas supply. Tank pressure range of small liquid rocket engines is between $6bar$ and $172bar$. The storable liquids, monopropellants or stored cold gas are used in the SLRE. Combustion chamber pressure of SLRE ranges between $1bar$ and $21bar$. Time elapsed to reach the full thrust can be between $0.004s$ and $0.080s$ [SB01].

1.2 Additive manufacturing

Additive Manufacturing (AM) is a promising technology for fabricating a wide range of structures and complex geometries from three-dimensional (3D) CAD model data. The process consists of depositing successive layers of material, one layer on top of another. Additive Manufacturing provides significant advantages such as reduced lead time, reduction of mass, development of complex geometry and cost over traditional manufacturing for rocket engines etc. when compared to traditional manufacturing, additive manufacturing has [Gra21]

- Lead times reduced by 2 to 10 times,
- Cost reduced by more than 50%,
- GE announced the ability to obtain a combined cycle efficiency of 63% through optimizing the design of non-rotating components and fabricating through AM [HK18].

According to ASTM F42, the ASTM community identifies seven different technologies under Additive manufacturing. Based on the requirement of this project, so-called powder bed fusion or selective laser melting (SLM), belonging to the group of AM processes was selected [Bla+21], [Ant22].

1.2.1 Selective Laser Melting (SLM)

In the SLM process, a powder layer (powder bed) is selectively exposed to a high-power laser beam (see Figure 1.1). A scanner system moves the focus point of the laser according to the contour of the desired part. The powder is locally melted, and the powder particles are bonded to each other. After this procedure, the build platform is lowered, and a new powder layer is applied with a recoater system (see Figure 1.1) [Til+17]

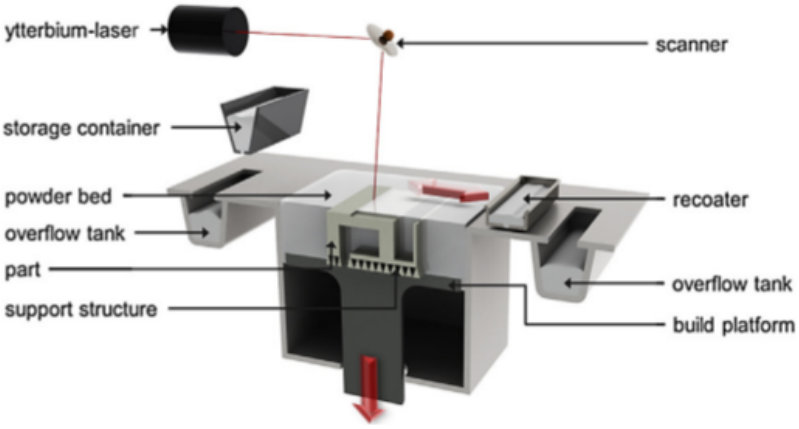

Figure 1.1: SLM Process Sketch

Subsequently, the new powder layer is selectively exposed to the laser. This procedure is repeated until the complete height of the part is obtained. The entire process takes place in an argon-filled chamber to avoid oxygen and nitrogen contamination of the processed metal. The main advantages of SLM are the wide range of possible geometries [Appendix 1], the high flexibility of metallic feedstock powders, the realization of inner structures with additional functions, better surface finish than DED, good trade-off between high precision and low deposition rate. Since the requirement of this project is to develop a 100N thrust Liquid propulsion System; high precision, smooth surface finish and ability to print designs with minimal size and thickness were some of the priorities. These requirements were satisfied better by SLM than DED comparatively.

Moreover, "Cold spray" is one of the potential AM techniques which can also be used for the development of Aerospace components. For example, recently NASA has performed a hot fire test in a cold spray produced liquid engine combustion chamber. The cold spray methodology offers a lot of advantages like avoiding roughness problems in the cooling channel, avoiding the problem of shrinkage and decreasing the cost [Gra+21]. However, if the ambient conditions and gases used during the cold spray methodology are not ideal, there is a risk of inferior material qualities [Per+21].

Commonly used SLM powder materials are Ni-based superalloys, Fe-alloys, and Ti-alloy. Inconel 718/IN718 is one Ni-based superalloy commonly employed for high temperature applications. Its superior mechanical properties, such as the high temperature strength and outstanding creep behaviour, are mainly based on solid solution strengthening and precipitation strengthening. It can withstand loading at an operating temperature close to its melting point of $1336°C$ [Yon+20].

1.3 Development Of Inconel 718 Based Liquid Propulsion System Using SLM Technique

Development of Aerospace components, small scale LRE, sensors etc using Additive manufacturing is becoming quite significant because of its numerous benefits. The SLM Solution and Cellcore have manufactured a downscaled LRE in SLM 280 PRODUCTION SERIES [SLM] which is a third-generation machine, featuring multiple lasers, closed-loop powder handling and upgraded process control ideal for demanding applications requiring high productivity with Inconel 718 using SLM A.M technique (Appendix C).

The SLM technique has proven to be a "Simplified manufacturing technique" (i.e.) Only minimal post-processing is needed despite the complex structure, this avoids tool wear when processing nickel-based alloy (IN718) which is generally too difficult to be machined. [Yon+20]. Moreover, some of the characteristics listed in the below Table 1.1 illustrates the high precision, production capabilities, surface finish and repeatability of SLM technique [Don19].

Table 1.1: The characteristic of SLM technique

S.no	Parameters	Value
1.	Maximum Build Volume	$(600 * 400 * 500)mm^3$
2.	Tolerance	$\pm 0.02mm$
3.	Minimum layer thickness	$0.03mm$
4.	Surface Roughness	$4 - 10\ \mu m$

Chapter 2

Design and Performance Evaluation

2.1 Design Requirements

The nominal design of the rocket engine considered the following constraints:

- Nominal thrust: $T = 100N$
- Expansion ratio : $\varepsilon = 80$ vacuum exhaust
- Burning time: $t_b = 100s$
- Combustion chamber pressure: $P_{CC} = 20bar$
- During firing, thrust decay should not exceed 50% of the initial nominal thrust
- Design should be compatible with additive manufacturing technology
- Construction of combustion chamber: Inconel 718 with additive layer manufacturing
- Rest of components (pipes and tanks): stainless steel AISI 316
- The hydraulic circuit is made by an open-close valve (no throttling capability) and a checkvalve
- The fuel is RP1 and oxidizer is 87.5% H_2O_2 and 12.5% H_2O.

2.2 Nominal Thermodynamic Parameters

The optimal $\frac{O}{F}$ ratio has been found using the `NASA CEA` code's *Assigned Enthalpy & Pressure* problem by retrieving T_{CC} and k and then calculate c^* to quantify the combustion efficiency. The reactants' initial temperature has been set to room temperature due to constraints from the code and the combustion chamber pressure to $P_{CC} = 20bar$. The $\frac{O}{F}$ ratio vs c^* curve can be seen in Figure 2.1 and the ratio was selected to $\frac{O}{F} = 7.5$ as it provides the highest efficiency. The obtained parameters are listed in Table A.1.

Table 2.1: Nominal thermodynamic parameters

$k[-]$	T_{CC} $[K]$	$M_{mol}[\frac{kg}{kmol}]$	c^* $[\frac{m}{s}]$
1.1346	2674	21.695	1594

2.3 Nominal Engine Design

Following the selection of $\frac{O}{F}$ and calculation of combustion parameters the rocket engine was sized to fulfill the requirements of t_b, minimum thrust during operation and compatibility with AM methods.

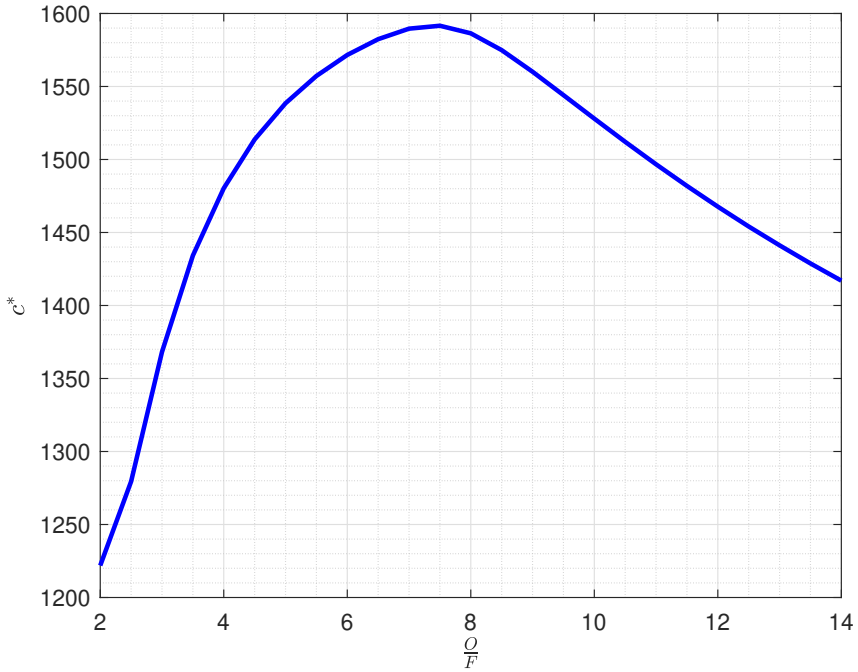

Figure 2.1: $\frac{O}{F}$ vs c^*

First of all, pressure ratio $\frac{P_e}{P_c}$ and c_T were calculated with Equation 2.1 and Equation 2.2.

$$\frac{1}{\varepsilon} = \left(\frac{k+1}{2}\right)^{\frac{1}{k-1}} \left(\frac{P_e}{P_{CC}}\right)^{\frac{1}{k}} \cdot \sqrt{\frac{k+1}{k-1}\left[1 - \left(\frac{P_e}{P_{CC}}\right)^{\frac{k-1}{k}}\right]} \tag{2.1}$$

$$c_T = \lambda \cdot \sqrt{2 \cdot \frac{k^2}{k-1} \cdot \left(\frac{2}{k+1}\right)^{\frac{k+1}{k-1}}} \cdot \sqrt{1 - \frac{P_e}{P_{CC}}^{\frac{k-1}{k}}} + \varepsilon \cdot \frac{P_e - P_a}{P_{CC}} \tag{2.2}$$

Then the throat area and exit area were found with Equation 2.3 and Equation 2.4.

$$A_t = \frac{T}{P_{CC}\ C_T} \tag{2.3}$$

$$A_e = \varepsilon\ A_t \tag{2.4}$$

The nozzle was designed using Rao approximation, with 100% length of a conical nozzle with $\alpha = 15°$, in order to minimize the thrust losses. From the Rao tables, the angles $\theta_e = 4.6°$ and $\theta_i = 31.2°$ were retrieved, so the length of the divergent part of the nozzle was calculated using Equation 2.5

$$L_{div} = \frac{r_e - r_t}{tan(\alpha)} \tag{2.5}$$

The mass flow rate was found from Equation 2.6, then the oxidizer and fuel mass flow rates were found based on the $\frac{O}{F}$.

$$\dot{m} = \frac{P_{CC}\ A_t}{c^*} \tag{2.6}$$

For the combustion chamber design, the characteristic length was retrieved from Humble [LHH95] and was found to be $L^* = 1.73m$. Then the volume was found as $V_c = L^* A_t$ and the cross sectional area with Equation 2.7. The convergent part of the nozzle was found using Equation 2.8, with assumed $\beta = 45°$ as it is a standard value.

$$A_c = \frac{A_t}{M_c}\left[\left(\frac{2}{k+1}\right)\left(1 + \frac{k-1}{2}\ M_c^2\right)\right]^{\frac{k+1}{2(k-1)}} \tag{2.7}$$

$$L_{conv} = \frac{r_c - r_t}{tan(\beta)} \tag{2.8}$$

To design the injection head, it was chosen to have short tubes with conical entrance injectors in 'unlike' configuration with 2 oxidizer and 1 fuel due to the mass flow rate differences. For fuel, it was decided to start with an orifice with a diameter $d_{RP1} = 0.5mm$ for the injector, due to the low mass flow rate, and that comes with a discharge coefficient $C_D = 0.7$. The needed area for fuel injection was then computed using Equation 2.9, where $\Delta P_{inj} = 0.2 P_{CC}$:

$$A_{inj,RP-1} = \frac{\dot{m_{fu}}}{C_D \sqrt{2 \Delta P_{inj}} \rho_{RP-1}} \tag{2.9}$$

The area of a single injector was computed using the chosen diameter so the number of needed fuel injectors could be retrieved. The obtained value was rounded to the closest integer and then used to re-compute the diameter necessary to obtain the correct mass flow rate. For the oxidizer the needed number of orifices was imposed by the chosen impinging configuration (double of the fuel orifices), knowing that the oxidizer orifices' diameter was evaluated. The values obtained are reported in Equation 2.3

Table 2.2: Injection head data, N_{inj} = number of injectors, d = diameter of orifices

	Fuel	Oxidizer
N_{inj}	1	2
d	0.532 mm	0.83 mm

The feed line diameters were found by first assuming a velocity of $U_f = 1 \frac{m}{s}$ in the pipes in order to limit losses and have a sufficiently large diameter to be easily procurable - as the mass flow rates are small. Then, from the mass flowrates the diameters were found by rounding their value to the closest manufacturable dimension - for example, $d = 0.3mm$ instead of $d = 0.29mm$.

The needed oxidizer and fuel mass were computed assuming a constant mass flow rate and accounting for a 10% margin related to the liquid that remains in the feeding line and cooling system after the firing:

$$m_{ox} = 1.1 \; t_b \; \dot{m}_{ox} \tag{2.10}$$

$$m_{fu} = 1.1 \; t_b \; \dot{m}_{fu} \tag{2.11}$$

knowing the mass and the fuel and oxidizer density the volume occupied by fuel and oxidizer was evaluated. The initial pressure of the tanks was retrieved by adding the losses due to the cooling, injectors, valves and feeding lines to the nominal combustion chamber pressure: $P_{fuel,i} = 27.15bar$ and $P_{oxidizer,i} = 24.26bar$, a detailed explanation on how these losses are computed is provided in the section "Performance Losses".The final pressure was retrieved using the same losses and a final value of the combustion chamber pressure $P_{CC,f} = 14bar$ that was computed through Equation 2.3 assuming constant c_T and a final thrust of $T = 70N$, the final tanks pressure obtained are: $P_{fuel,f} = 21.15 \; bar$ and $P_{oxidizer,f} = 18.26 \; bar$. With that data the needed volume and mass of pressurant (N_2) were retrieved by assuming that it expands adiabatically during the firing. From that it was possible to compute the total volume of the tanks as a sum of the fuel/oxidizer and pressurant volume: $V_{TANK_{OX}} = 0.0119 \; m^3$ and $V_{TANK_{RP-1}} = 0.0042 \; m^3$. Having decided to use spherical tanks and knowing the volume, it was possible to retrieve the radii: $r_{TANK_{RP-1}} = 0.10m$ and $r_{TANK_{OX}} = 0.142m$. The thickness was computed to withstand a burst pressure 2 times higher than the initial pressure with Equation 2.12:

$$t_{TANK} = \frac{P_{burst} \cdot r_{TANK}}{2 \; F_{ut_{AISI316}}} \tag{2.12}$$

where $F_{ut_{AISI316}}$ is the ultimate tensile strength of AISI316. Finally we estimated the mass of the tanks using the following relation:

$$M_{TANK} = A_{TANK} \cdot t_{TANK} \cdot \rho_{AISI316} \tag{2.13}$$

in which A_{TANK} is the surface area of the tank, the values we computed are: $M_{TANK_{RP-1}} = 4.74kg$ and $M_{TANK_{OX}} = 8.4kg$

Performance Losses

The performance losses due to heat addition were accounted with the `NASA CEA` code using the finite area rocket problem and the divergence losses in the nozzle with Equation 2.14.

$$\lambda = \frac{1}{2}\left(1 + cos\frac{\alpha + \theta_e}{2}\right) \tag{2.14}$$

The pressure losses due to injection plate were sized as $\Delta P_{inj} = 0.2\ P_{CC}$ and due to the cooling system as $\Delta P_{cool} = 0.15\ P_{CC}$, as it was suggested by Humble [LHH95]. The feeding line losses were modeled as Equation 2.15, where f_p is the pipe's friction coefficient and the losses due to the presence of the valves as Equation 2.16.

$$\Delta p_p = \frac{1}{2}\ \frac{f_p L_p}{D_p}\ \rho\ U_f^2 \tag{2.15}$$

$$\Delta p_v = \frac{1}{2}\ k_v\ \rho\ U_f^2 \tag{2.16}$$

Then, in order to model the transient effects the losses were written in the following form Equation 2.17, where i is the index of a component causing the loss and j is either the fuel or oxidizer volumetric flow rate $Q_j = U_{f,j} A_{p,j}$.

$$\Delta p_{ij} = K_i\ Q_j^2 \tag{2.17}$$

2.4 Blow-Down Combustion Simulation

To evaluate how the performance of the engine changes in time, the evolution of the combustion of the blow-down system has been simulated. Due to the nature of the system, the pressure in the tanks **decreases** as the propellant is **burnt**. Starting from the nominal condition at $t = 0s$, at each time step, combustion chamber pressure, mass flow rate an $\frac{O}{F}$ are taken as inputs for the `NASA CEA` code to compute the **combustion properties** at the following instant. Computing also the mass variation of both fuel and oxidizer as shown in Equation 2.18, where i and $i-1$ identify two successive time steps, the new tanks' pressure can be calculated assuming an **adiabatic expansion** for N_2 gas.

$$\Delta M = \dot{m} \cdot (t_i - t_{i-1}) \tag{2.18}$$

With the new tanks' pressures and combustion chamber pressure, the new mass flow rates of fuel and oxidizer can be found running `pressureLossesRP1.m` and `pressureLossesOX.m`. With $\dot{m}_{RP-1}$ and $\dot{m}_{OX}$, the total mass flow rate and the oxidizer to fuel ratio at the new time instant are retrieved.

Finally, fixing the expansion ratio at $\varepsilon = 80$, having characterized the losses in the nozzle with the coefficient $\lambda = 0.9927$, knowing the updated values of $\dot{m}$, of the specific heat ratio k and of c^*, the **thrust coefficient** and the **thrust** are evaluated as in Equation 2.2 and Equation 2.19, [HP92, Ch. 11]:

$$T = \dot{m} \cdot c_T \cdot c^* \tag{2.19}$$

The procedure is repeated up to the final burning instant $t_f = 100s$, so that the complete evolution of the parameters is known. A better description of the algorithm is reported in Appendix B.
The results of the `LREburning.m` simulation are shown in Figure 2.2.

Combustion simulation The real values of characteristic velocity, c^*, were retrieved using the `NASA CEA` code running a `combustion` case[1]. This case computes the combustion chamber temperature, T_{CC}, the molar mass of the products, M_{mol} and the specific heat ratio of the exit gases, k[2]. Once these parameters are computed, the `cStar.m` function is called for the computation of the c^*.
The dimensions of the engine are found in Table A.1 in the appendix.

[1] All the `combustion` and `rocket` cases are set up using the official **NASA user-guide** [MG96].

[2] `writeCombustionFile.m` generates the `*.inp` file that is executed by the `NASA CEA` during the simulation at every time step iteration.

2.4.1 Requirement Verification

Following the completion of the design and modeling of the system, the nominal design was simulated in the transient code. Figure 2.2 shows the evolution of the relevant parameters during the burning time. The pressure losses due to heat addition, cooling and feeding system as well as thrust losses due to divergence were included in order to have a more realistic view of the performance.

The modelled design of the system respects the constraint of Selective Laser Melting A.M techniques Table 1.1. Especially, design of orifice and others miniature components of LRE were handled meticulously because of the critical constraint over the minimum building thickness, printing resolution and its uncertainties. **SLM 280 Production Series** [**SLM**] machine was selected for manufacturing the design modelled Figure C.3. Thus, machinability, accuracy, production capability etc. were respected and treated with higher tolerance to ensure the reliability of the product.

As both performance and manufacturing requirements were fullfilled, it can be concluded that the design process ended successfully.

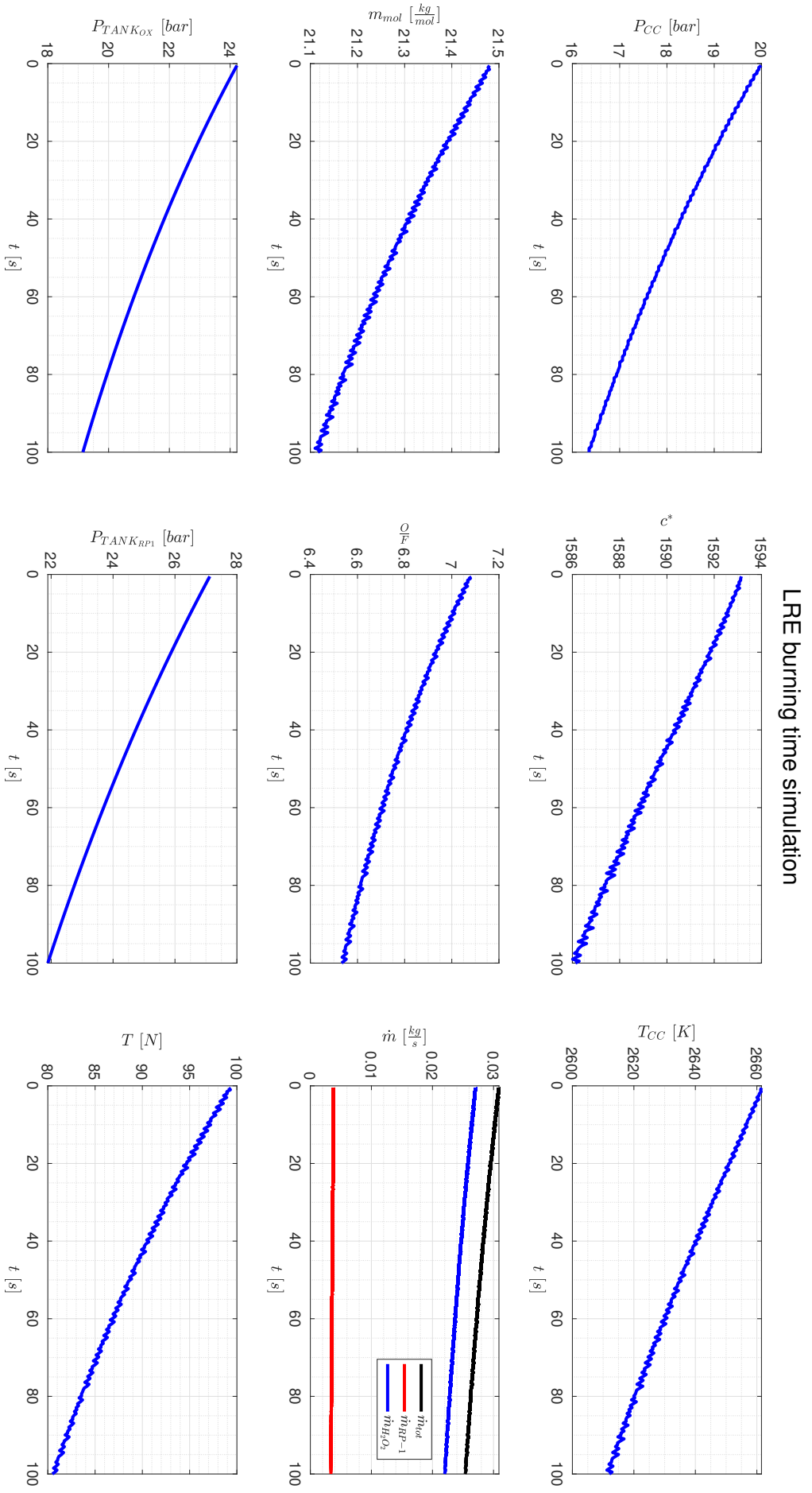

Figure 2.2: LRE burning evolution, blow down architecture.

Chapter 3

Uncertainty Analysis

There are "n" number of uncertainties which can possibly affect the functionality of the system. In this project, some of possible uncertainties from critical revision and literature where listed out and tabulated. To Identify the most critical uncertainty which affects the nominal thrust $100N$, a **novel filtration process** was developed and used.

3.1 Nominal Design Uncertainties

3.1.1 Preliminary Filtration: Based on the Impact on Nominal Thrust

This is the initial filtration process where the tabulated uncertainties are rated based on the direct influence on the nominal thrust Figure D.1. From this preliminary filtration, surface roughness, shrinkage, blown powder deposition and cavitation were chosen are highly influential uncertainties on the nominal thrust.

3.1.2 Secondary Filtration: Post Processing

In additive manufacturing, there are various types of defects, including pores, cracks, anisotropy, residual stresses, thermal stresses, laser spattering, and poor surface roughness. Different post-processing techniques, including laser shock peening, laser polishing, conventional machining, and heating processes, have been used to resolve these issues. These processes have proved their capability to improve the mechanical properties and reduce the residual stresses formation and surface finish of AM products.

- For complex parts with fine feature sizes, trapped powders can be a challenge to remove. Typical approaches involve rotational movements, tapping and blowing powders out of surface cavities and channels before the heat treatment process [Bla+21].
- The surface finish has a direct effect on the performance and fatigue strength [GPW19], [Til+17]. Laser polishing (LP) can decrease the surface roughness up to 95%. Conventional machining is also commonly applied to amplify surface characteristics such as surface roughness and skewness. Also, simple machining increases cavitation erosion resistance of superalloys manufactured by SLM [TM21], [Gon+15], [Bla+21].
- Thermal post-processing techniques have commonly been used to eliminate pores, enhance corrosion resistance, and improve mechanical properties. There are various thermal post-processing techniques: (a) solution heat treatment, (b) hot isostatic pressing, and (c) T6-heat treatment. For IN718 processed with SLM, the temperature should be higher than $1150°C$ and the pressure should be above 100 MPa to obtain a significant reduction of cavities. The relative density can be improved to 99.985% - 99.989% by HIP [Mah+22].
- Laser power, hatch spacing, and scanning speed has a direct influence on surface roughness. So optimal values for those parameters are $320W$ laser power, $600\frac{mm}{s}$ a scan speed, and 0.12 mm hatch spacing results in a relative density of 99.2% and relatively low surface roughness of $3.5\mu m$ [JG14], [Bal+20].
- As the increase of heat flux at the region just before the nozzle throat creates problems for the small liquid rocket engines, the addition of the ceramic coating around the throat can be considered.

Applying the secondary filtration, the critical uncertainties were shortlisted by surface roughness and Manufacturing shrinkage. The flowchart for the identification of critical uncertainty is attached in Figure D.2.

3.1.3 Ternary Filtration: Monte Carlo analysis

A **Monte Carlo** analysis has been conducted in order to understand the *impact* of the **manufacturing process** on the thrust, T.

Monte Carlo Analysis Steps

Taking into consideration the above qualitative results on the **additive manufacturing process**, one of the main parameters that can affect the LRE performance is the **manufacturing accuracy** of the injection plate, in particular the **injection holes**.

From the literature, it has been evinced that the **manufacturing tolerances** are around $\pm 2 \cdot 10^{-5}\ m$. Comparing these tolerances with the holes sizes, $\phi_{RP-1} \approx 8.3 \cdot 10^{-4}\ m$ and $\phi_{OX} \approx 5.2 \cdot 10^{-4}\ m$, it is soon spotted that the additive manufacturing process, used for the manufacturing of the injection plate, is **at its limit of applicability**.

The steps followed by the **Monte Carlo** simulation in `monteCarlo.m` are:

- Convert the **uncertainties** from the manufacturing process into **standard deviations** assuming a **gaussian distribution** of the variables, ϕ_{RP-1} and ϕ_{OX}.
- Loop study till convergence based on the relative error made on the computed thrust standard deviation and thrust mean value, σ_T and $\bar{T}$:
  - Compute, using the gaussian distribution, a new random value for ϕ_{RP-1} and ϕ_{OX}
  - Compute new **mass flow rates** knowing the initial tanks pressure and the combustion chamber pressure, $P_{TANK_{OX_{t=0}}}$, $P_{TANK_{RP-1_{t=0}}}$ and $P_{CC_{t=0}}$, using `pressureLossesOXMC.m` and `pressureLossesRP1MC.m`
  - Compute the new $\frac{O}{F}$ value using the above **mass flow rates**
  - Compute the thrust in vacuum, T, with the help of the `NASA CEA` code simulation, setting as input $\frac{O}{F}$, ε, $P_{CC_{t=0}}$, T_{RP-1} and T_{OX}. Furthermore, the real values of thrust, T, were retrieved using the `NASA CEA` code running a `rocket` case enabling the `frozen` option for the diverging part of the nozzle. This because it is supposed that the **chemistry time scale**, in the diverging part, is *higher* than the **flow time scale** in the diverging part of the nozzle[1]
  - Update the vector that stores all the previous computed thrust values, `Tvec`
  - Compute the new thrust mean value and the new thrust standard deviation, $\bar{T}$ and σ_T
  - Check if $\bar{T}$ and σ_T are both below the defined tolerances, `meanTol` and `deviationTol`

The results of `monteCarlo.m` are in Figure 3.1, where T is the instantaneous thrust computed at each Monte Carlo iteration, $\bar{T}$ is the mean value of `Tvec`, σ_T is the standard deviation of `Tvec` and the $\dot{m}$ are the mass flow rate that change because the randomness on the holes diameter, ϕ_{OX} and ϕ_{RP-1}.

Monte Carlo Results

Based on the **random** analysis it is clear that the **manufacturing process** (Shrinkage) have affects very much the **thrust capabilities** of the 100 N liquid rocket.

This because the **maximum accuracy** of the **manufacturing process** is **one order of magnitude lower** than the **oxidizer** and **RP-1 injector holes' diameter**. These extreme **manufacturing** conditions can have serious implication on the working of the rocket: a *small* **fluctuation** on the injector holes' **diameter** can result in a *huge* variation on the **mass flow rate**[2] that will result in a *huge* variation in the **thrust**. This will result in a *huge* **variation from the ideal working conditions**. So,it is conclusive that Shrinkage in diameter of the orifice caused during the manufacturing process has more negative influence on nominal thrust than the Surface roughness which is in the order of micrometres.

[1] `writeFile.m` generates the `*.inp` file that is executed by the `NASA CEA` during the simulation at every Monte Carlo iteration.

[2] Both for oxidizer and fuel.

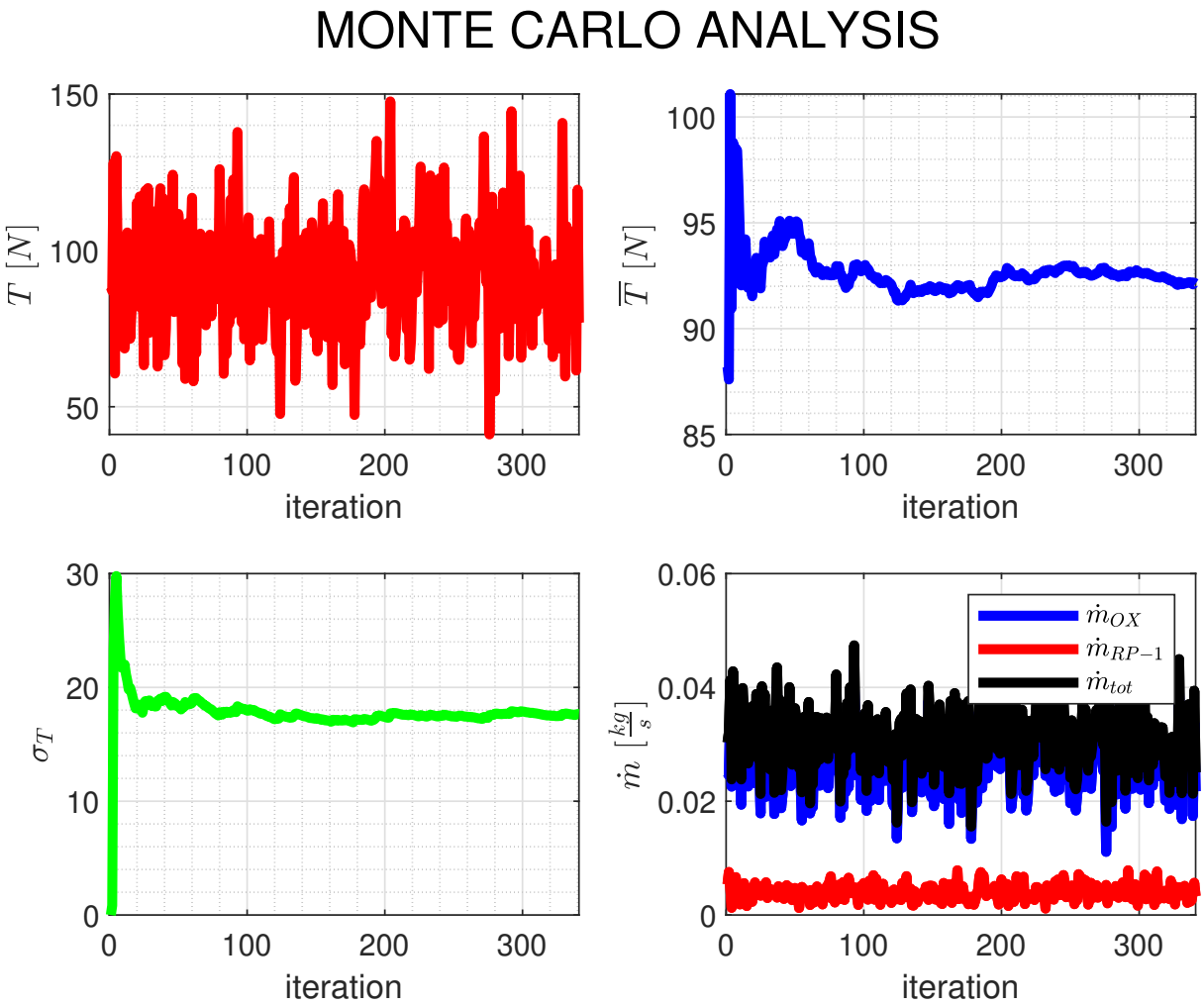

Figure 3.1: Monte Carlo analysis results.

3.2 Critical Observation for the $10N$ and the $1000N$ Rockets

Considering that the LRE (both downscaled and upscaled version) is developed using Selective Laser Melting Additive Manufacturing (SLM AM) technique using SLM 280 production machine and Post processing (laser polishing, heat Treatment and HIP) was performed to the developed Models.

In order to attain the thrust according to the below mentioned two cases, the diameter of the orifice is varied, to control the mass flow rate of the fuel and oxidizer entering the combustion chamber.

3.2.1 Case 1: The 10N Thrust LRE

For the scenario 1; the influence of the uncertainty - especially manufacturing uncertainties (shrinkage) and surface roughness - will be a critical issue. For the down-scaled version of 10N LRE, the miniature geometry, such as diameter of the orifice and the injector duct, will be difficult to manufacture using SLM technique with high precision and smooth surface finish because of its production constraints. The manufacturing uncertainties can critically affect the performances and impact of surface roughness is not small (negligible) anymore in the 10N LRE.

3.2.2 Case 2: The 1000N Thrust LRE

In this up-scaled version of 1000N LRE, the influence of uncertainties such as shrinkage during manufacturing process and surface roughness will have less influence on the performance. But build envelope (max. building volume) constraint might be one of the potential hindrance for the manufacturing of 1000N LRE. As the dimension of the model increases, the structural problem becomes more influential than the

fluid dynamic problem. So, the mechanical properties,Local relative density, fatigue, micro-structure of Inconel 718 etc will have higher impact in this scenario.

Chapter 4

Conclusion

In conclusion, the design process of the nominal rocket was presented as well as the operational simulation in order to prove the fulfillment of the design requirements. The Monte Carlo simulations showed that when accounting for the uncertainties the design is robust and still fulfills the requirements, the mean uncertain performance is close to the nominal performance. The possibilities of down- and upsizing were also discussed as well as their implications on the performance uncertainties.

Bibliography

[HP92] Philip G Hill and Carl R Peterson. "Mechanics and thermodynamics of propulsion". In: *Reading* (1992).

[LHH95] Wiley J Larson, Gary N Henry, and Ronald W Humble. *Space propulsion analysis and design*. McGraw-Hill, 1995.

[MG96] Bonnie McBride and Sanford Gordon. "Computer Program for Calculation of Complex Chemical Equilibrium Compositions and Applications". In: (1996).

[SB01] George P Sutton and Oscar Biblarz. "Rocket Propulsion Elements JOHN WILEY SONS". In: *Inc., New York* (2001).

[JG14] Qingbo Jia and Dongdong Gu. "Selective laser melting additive manufacturing of Inconel 718 superalloy parts: Densification, microstructure and properties". In: *Journal of Alloys and Compounds* 585 (2014), pp. 713–721.

[Gon+15] Xibing Gong et al. "Characterization of microstructure and mechanical property of Inconel 718 from selective laser melting". In: *International Manufacturing Science and Engineering Conference*. Vol. 56826. American Society of Mechanical Engineers. 2015, V001T02A061.

[Til+17] Wolfgang Tillmann et al. "Hot isostatic pressing of IN718 components manufactured by selective laser melting". In: *Additive Manufacturing* 13 (2017), pp. 93–102.

[HK18] Ahmed Arabi Hassen and Michel M Kirka. "Additive Manufacturing: The rise of a technology and the need for quality control and inspection techniques". In: *Materials Evaluation* 76.4 (2018), pp. 438–453.

[Don19] Steffen Donath. *3D Printing a Rocket Engine*. 2019. URL: https://www.etmm-online.com/3d-printing-a-rocket-engine-a-886960/. (accessed: 19.05.2022).

[GPW19] Paul R Gradl, Christopher S Protz, and Tal Wammen. "Additive manufacturing and hot-fire testing of liquid rocket channel wall nozzles using blown powder directed energy deposition inconel 625 and JBK-75 Alloys". In: *AIAA Propulsion and Energy 2019 Forum*. 2019, p. 4362.

[Bal+20] Mohamed Balbaa et al. "On selective laser melting of Inconel 718: Densification, surface roughness, and residual stresses". In: *Materials & Design* 193 (2020), p. 108818.

[Yon+20] Ching Kiat Yong et al. "A critical review of the material characteristics of additive manufactured IN718 for high-temperature application". In: *Metals* 10.12 (2020), p. 1576.

[Bla+21] Byron Blakey-Milner et al. "Metal additive manufacturing in aerospace: A review". In: *Materials & Design* 209 (2021), p. 110008.

[Gra21] Paul Gradl. "Principles of Directed Energy Deposition for Aerospace Applications". In: (2021).

[Gra+21] Paul R Gradl et al. "Advancing GRCop-based Bimetallic Additive Manufacturing to Optimize Component Design and Applications for Liquid Rocket Engines". In: *AIAA Propulsion and Energy 2021 Forum*. 2021, p. 3231.

[Per+21] Lorena Perez et al. "Cold Spray Deposition of Heat-Treated Inconel 718 Powders". In: *ITSC2021*. ASM International. 2021, pp. 171–176.

[TM21] Gabriel Taillon and Kazuyoshi Miyagawa. "Cavitation Erosion of Ni-Based Superalloys Manufactured by Forging and Additive Manufacturing". In: *Journal of Failure Analysis and Prevention* 21.5 (2021), pp. 1902–1917.

[Ant22] Paolo Betteni Antonio M. Grande. "Additive Manufacturing". In: *Lecture Note of Aerosapce Material and Technology* (2022).

[Mah+22] Muhammad Arif Mahmood et al. “Post-Processing Techniques to Enhance the Quality of Metallic Parts Produced by Additive Manufacturing”. In: *Metals* 12.1 (2022), p. 77.

[SLM] SLM. *Highly Productive 3D Printer*. URL: https://www.slm-solutions.com/products-and-solutions/machines/slm-280-production-series. (accessed: 19.05.2022).

Appendix A

Nominal Design

Table A.1: Engine dimensions

$V_{ox}[m^3]$	$V_{fu}[m^3]$	$d_{inj}^{ox}[mm]$	$d_{inj}^{fu}[mm]$	$L_c[cm]$	$A_c[cm^2]$	$A_t[cm^2]$	$L_{div}^{nozzle}[cm]$	$L_{conv}^{nozzle}[cm]$	$A_e[cm^2]$
0.0119	0.0042	0.83	0.53	25.34	1.48	0.246	8.3	0.41	19.69

Appendix B

Time Marching Code Description

The time analysis of the system has been made with a **time advancing method**. All the steps needed for the time simulation are stored into `LREburning.m`. The program works executing the following steps:

- Compute the new **chamber pressure**, P_{CC_i} using the previous time step **mass flow rate**, $\dot{m}_{OX_{i-1}}$ and $\dot{m}_{RP-1_{i-1}}$, **oxidizer to fuel ratio**, $\frac{O}{F}_{i-1}$, and the previous **combustion chamber pressure**, $P_{CC_{i-1}}$
  - c^* computation calling the `NASA CEA` code
  - P_{CC_i}[1] computation as $P_{CC_i} = \frac{c^* \ \dot{m}_{tot}}{A_t}$.
- Compute the new **tank pressure**, $P_{TANK_{OX_i}}$ and $P_{TANK_{RP-1_i}}$. Each tank pressure is computed from a decrement of **propellant volume** and assuming an **adiabatic expansion** of the **nitrogen**
- Compute the new time step **mass fluxes**, $\dot{m}_{OX_i}$ and $\dot{m}_{RP-1_i}$, using the computed **losses coefficients** and the **new pressure variation** between the two propellant tanks and the combustion chamber, $\Delta P_{RP-1_i} = P_{TANK_{RP-1_i}} - P_{CC_i}$ and $\Delta P_{OX_i} = P_{TANK_{OX_i}} - P_{CC_i}$
- Thrust, T_i, computation using the new **ith** variables and the **3D nozzle losses**, λ

A flow chart of the code is showed in Figure B.1:

[1] Corrections are made in order to avoid the new time step combustion chamber pressure to diverge.

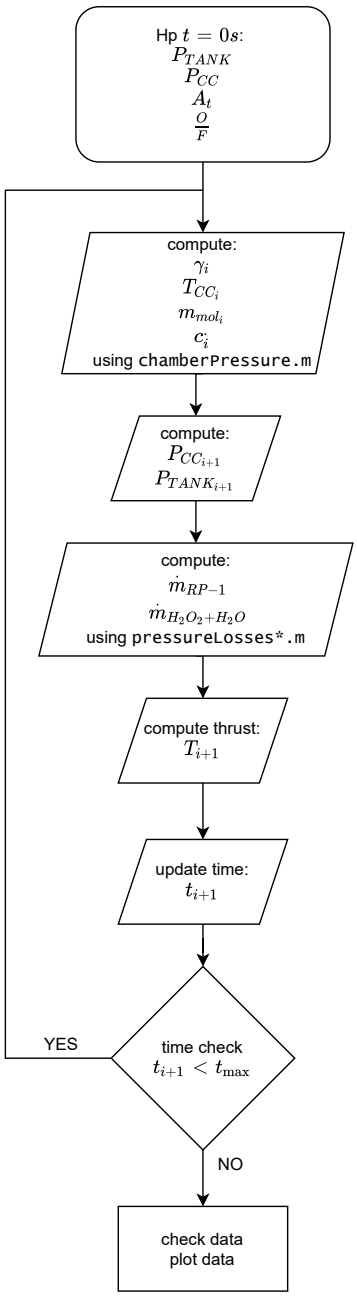

Figure B.1: `burningEvolution.m` flow chart.

Appendix C

Selective Laser Melting

1. The Comparative chart on precision vs deposition rate and feature size for different AM technique

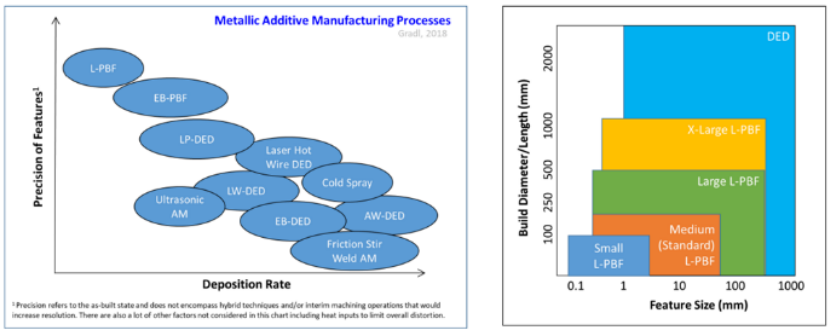

Figure C.1: Precision Vs Deposition Rate and Wide Range of Sizes

2. The SLM 280 production Series and its product (Source: SLM)

Figure C.2: SLM 280 processing series(left) and SLRE developed by SLM solution(right)(Source: SLM)

3. The SLM 280 production Series Specifications)

Build Envelope (L x W x H):	280 x 280 x 365 mm 11 x 11 x 14 in (reduced by substrate plate thickness)
3D Optics Configuration:	Single (1x 400 W or 1x 700 W) IPG fiber laser Twin (2x 400 W or 2x 700 W) IPG fiber laser Dual (1x 700 W and 1x 1000 W) IPG fiber laser
Build Rate:	up to 113 cm^3/h (Twin 700 W)
Variable Layer Thickness:	20 µm - 90 µm (more upon request)
Minimum Feature Size:	150 µm
Beam Focus Diameter:	80 µm - 115 µm
Maximum Scan Speed:	10 m/s
Average Inert Gas Consumption in Process:	13 l/min (argon)
Average Inert Gas Consumption Purging:	160 l/min (argon)
E-Connection / Power Input:	400 Volt 3NPE, 63 A, 50/60 Hz, 3.5-5.5 kW
Compressed Air Requirement / Consumption:	ISO 8573-1:2010 [1:4:1], 60 l/min @ 6 bar
Dimensions (L x W x H):	4150 mm x 1200 mm x 2525 mm (includes PSV)
Weight:	1700 kg dry 2600 kg with powder

Figure C.3: The SLM 280 production Series Specifications

Appendix D

The Uncertainty Analysis

1. The Uncertainty Analysis chart

S.no	Application	A.M. Technique	List of uncertainties	Outcomes of the uncertainties	Actions (Post processing)	Impact of uncertainty on Nominal Thrust	Comment
1	Design and development of a new Liquid Propulsion family	Selective Laser Melting (L-PBF)	Shrinkage (Manufacturing Process)	Surface Morphology defect	conventional machining techniques / thermal processes	5	tolerance of +/-0.02 mm deviation
			Open pores	Formation of interlayer voids / entrapment of gas particles	Hot Isostatic pressing	3	microscopic defects
			Balling effect defect	Surface integrity and densification Issues		2	
			Surface Roughness	Variation in Mass Flow Rate / Variation in Discharge Coef.	Laser polishing	5	Ra varies from 4 to 10 micrometre
			Local Cavitation	Variation in Mass Flow Rate / Variation in Discharge Coef.		4	Variation in discharge coefficient is below 4% for injectors and below 3% for the oxidizer injectors.
			Porosity	Fatigue Issues / initiation of crack	Hot Isostatic pressing / Solution Heat treatment	1	variation in mechanical property
			Surface Residual Stress	Fatigue failure		2	
			Local relative Density	Anisentropic behaviour		2	
			Blown powder deposition	Internal fusing within the hot flow channel	Blown powder cleaning processing	4	5% to 10% of the excessive powder should be removed from the channel

Figure D.1: Uncertainty Analysis chart

2. The flowchart for the identification of critical uncertainty

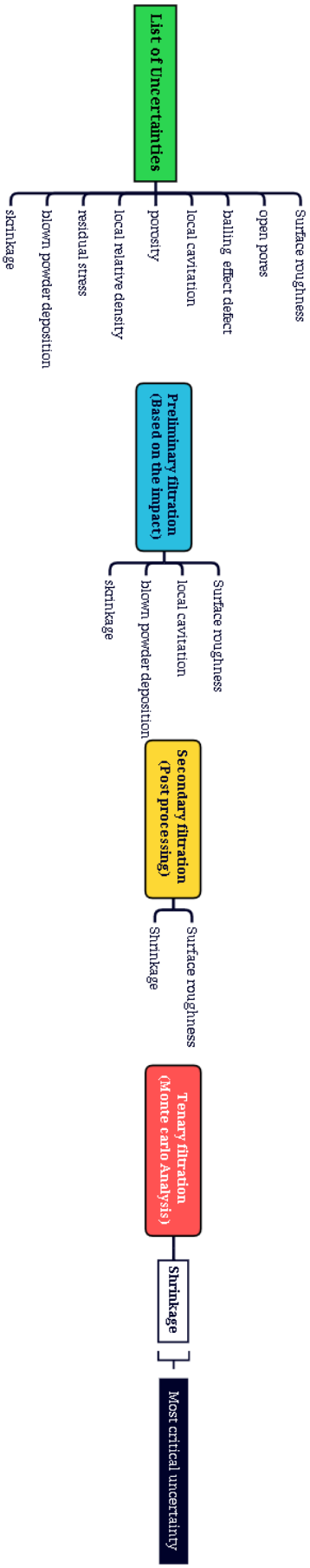

Figure D.2: flowchart for the identification of critical uncertainty